Enhancing proton exchange membrane water electrolysis by building electron/proton pathways

Liyan Zhu [a], Hao Zhang [a], Aojie Zhang [a], Tian Tian [a,b,**], Yuhan Shen [a], Mingjuan Wu [a], Neng Li [a,*], Haolin Tang [a,b,c,***]

[a] State Key Laboratory of Advanced Technology for Materials Synthesis and Processing, State Key Laboratory of Silicate Materials for Architectures, Wuhan University of Technology, Wuhan 430070, China
[b] National Energy Key Laboratory for New Hydrogen-ammonia Energy Technologies, Foshan Xianhu Laboratory, Foshan 528200, China
[c] Hubei Key Laboratory of Fuel Cell, Wuhan 430070, China

ARTICLE INFO

ABSTRACT

Proton exchange membrane water electrolysis (PEMWE) plays a critical role in practical hydrogen production. Except for the electrode activities, the widespread deployment of PEMWE is severely obstructed by the poor electron-proton permeability across the catalyst layer (CL) and the inefficient transport structure. In this work, the PEDOT:F (Poly(3,4-ethylenedioxythiophene):perfluorosulfonic acid) ionomers with mixed proton-electron conductor (MPEC) were fabricated, which allows for a homogeneous anodic CL structure and the construction of a highly efficient triple-phase interface. The PEDOT:F exhibits strong perfluorosulfonic acid (PFSA) side chain extensibility, enabling the formation of large hydrophilic ion clusters that form proton-electron transport channels within the CL networks, thus contributing to the surface reactant water adsorption. The PEMWE device employing membrane electrode assembly (MEA) prepared by PEDOT:F-2 demonstrates a competitive voltage of 1.713 V under a water-splitting current of 2 A cm^{-2} (1.746 V at 2A cm^{-2} for MEA prepared by Nafion D520), along with exceptional long-term stability. Meanwhile, the MEA prepared by PEDOT:F-2 also exhibits lower ohmic resistance, which is reduced by 23.4 % and 17.6 % at 0.1 A cm^{-2} and 1.5 A cm^{-2}, respectively, as compared to the MEA prepared by D520. The augmentation can be ascribed to the superior proton and electron conductivity inherent in PEDOT:F, coupled with its remarkable structural stability. This characteristic enables expeditious mass transfer during electrolytic reactions, thereby enhancing the performance of PEMWE devices.

1. Introduction

Hydrogen has been received prevailing attention as a renewable, eco-friendly, and decarbonizing energy carrier [1]. Among various electrolysis technology for hydrogen production, proton exchange membrane water electrolysis (PEMWE) is more appealing for practical applications with certain advantages, such as high hydrogen purity, short reaction time, and superior stability [2,3]. As the pivotal component determining the electrolyzer's performance, the membrane electrode assembly (MEA) encompasses membranes and catalyst layer (CL). Classified based on their function, membranes can be categorized into cation exchange membranes (CEM) that are selective for cations, anion exchange membranes (AEM) that are selective for anions, and bipolar membranes, which combine the selectivity of both CEM and AEM [4–10]. PEMWE employs the proton exchange membrane, also referred to as CEM, that exhibits selectivity towards protons [11,12]. While the CL, composed of catalysts and ionomers, serves as the site for direct electrochemical reactions. It is worth noting that the precondition for electrochemical reactions to occur is that the three-phase boundary theory is satisfied [13]. However, the sluggish kinetics of multistep-coupled oxygen evolution reaction (OER) at anode CL usually leads to a considerably high overpotential, which in turn causes a significant voltage loss in the

electrolyzer and then hinders the overall PEM device performance [14–18]. Moreover, high-quality catalyst layer (CL) is one of the most essential factors contributing to the construction of superior electrode interfaces [19–22]. Exceptional co-conductivity between electron and proton facilitates the formation of active OER catalyst sites and the crossing of CL, which is crucial for the enhancement of catalyst activity and water electrolysis efficiency, especially when low-conductivity earth-abundant catalysts are applied.

Currently, great effort has been devoted in providing better electrical contacts and higher utilization efficiency by introducing conductive substrates (C, Ti, Sn-based materials) to achieve a larger active area [20, 23–28]. However, most of these research efforts failed to assess the efficacy of MEA. It has also been demonstrated that the sheet conductivity of CLs could be greatly improved by the introduction of conductive (Au, Ag, CNT) nanolayers, which facilitates the efficiency of catalyst utilization [21,29–32]. Although the resistance of CLs can be significantly reduced, a poorly coordinated introduction of conductive nanolayers may hinder proton transport between CL and the proton exchange membrane, which in turn reduces the efficiency of water electrolysis. In addition to metallic materials, the use of conducting polymers (CPs) as promising candidates for catalyst supports has been also investigated. CPs/catalyst-nanoparticle composites facilitate the easy charge flow through the polymer matrix during electrochemical processes, thereby accelerating electron transfer between the catalyst and the substrate [33]. Unfortunately, it remains unclear how electronic conductivity and CL conductivity interact in OER process.

In conventional CLs, ionomers can homogeneously integrate the catalyst particles, thereby providing proton transport pathways for the network structure within the catalyst layer [34–37]. The incorporation of ionic polymer (Nafion (PFSA)) enhances the proton conductivity, while it also tends to decrease the porosity of CL to some extent, thus impeding both mass transport and electron conductivity [38]. It has been demonstrated that the sheet resistance of CLs plays a significant role in boosting OER active sites [39]. Alternatively, Nafion phase within CL can be removed thoroughly as a means of further optimizing performance if both electron and proton conductivity are achieved. In this case, only two-phase boundaries are theoretically required for electron and ion transfer compared to the triple-phase boundaries required for OER procedure. Among numerous conductive polymers (CPs), representative polypyrrole (PPy), polyaniline (PANI), and poly(3, 4-ethylenedioxythiophene) (PEDOT) have been extensively studied [33]. In particular, PEDOT has been attracting increasing attention due to its advantages such as superior chemical stability, excellent electrical conductivity, and simplicity of fabrication [40–43]. The dispersibility of PEDOT is dependent on the polymer counterion, which forms a coulombic interaction with it. As a general candidate for polymer counterion, polystyrene sulfonic acid (PSS) has been extensively researched and applied as MPEC due to its exceptional solubility and compatibility [44–47]. In addition, perfluorosulfonic acid (PFSA) can also be incorporated with PEDOT to form MPEC for electron and proton conduction, respectively.

In this work, MPEC PEDOT:F was prepared by polymerizing monomeric EDOT onto a PFSA template. Since PEDOT is a conjugated polymer, its conjugated backbone allows free electrons to be easily transported through the π-orbital system and can therefore be used for electron conduction [46]. In addition, the portion of the PFSA that is not involved in stabilizing the PEDOT is used for proton transport via the Grotthuss mechanism [48], resulting in a superior co-conductivity of electrons and protons for an efficient PEMWE electrode. The functional role of MPEC PEDOT:F was elucidated through physical characterization and electrochemical tests. Founded on the imperative of ensuring proton conduction, the electronic conductivity of PEDOT contributes to improve the electron transfer ability, thus contributing to the mass-transfer process of the catalytic reaction, exhibiting excellent electrochemical properties. Density Functional Theory (DFT) calculations indicate that PEDOT:F facilitates the enhancement of electron transfer capacity and increased

exposure of active sites, thus resulting in a large number of active sites and excellent OER electrochemical properties.

2. Results and discussion

As illustrated in Fig. 1a, the monomer EDOT oxidatively polymerizes on the PFSA template to form PEDOT:F polymers [44]. Fig. 1b illustrates the schematic of theMEA with PEDOT:F and conventional Nafion as catalyst binders in CL. PEDOT:F serves as a mixed proton-electron conductor binder, employed for co-conduction of both protons and electrons. This co-conduction enhances the electron transfer capacity in comparison to the CL with proton-conducting, electron-insulating materials such as Nafion. Furthermore, PEDOT:F possesses significant dissimilar charges, facilitating its dispersion in solution and fostering the establishment of effective triple-phase boundaries for the expeditious mass transfer during the electrolytic reaction process in the CL, thereby augmenting the performance of PEMWE.

Fig. 2a display the S 2p signals in the X-ray photoelectron spectra corresponding to different ratios of PEDOT:F. Owing to the disparate binding energies of S in PEDOT and PFSA, the S in PFSA manifests as the SO_3H group at a higher binding energy (BE) in XPS, while in PEDOT, it adopts the form of thiophene at a lower BE. The XPS bands within the range of 166–172 eV are attributed to the sulfonate moieties ($-SO_3H$) of PFSA, while those within the range of 163–166 eV are assigned to the sulfur atoms ($-S-$) of the thiophene moiety in PEDOT. Consequently, the ratio of sulfonate moieties to thiophene moiety ($R_{S/T}$) in PEDOT:F can be inferred from the positions of the distinct BE of S 2p (where S represents SO_3H in PFSA and T represents thiophene in PEDOT). The $R_{S/T}$ values for the five prepared samples of PEDOT:F-1, PEDOT:F-2, PEDOT:F-3, PEDOT:F-4, and PEDOT:F-5 are 1/1.67, 1.03/1, 3.75/1, 4.25/1, and 5.35/1, as illustrated in Fig. S1. The structural characteristics of PEDOT:F and PFSA were analyzed via FTIR, as depicted in Fig. 2b. The concentrated peaks at 1210 and 1142 cm^{-1} correspond to the stretching vibrations of the C—F and S—O bonds of PFSA. The peak at 1052 cm^{-1} of PFSA is attributed to the symmetric stretching of the sulfonate moieties. In the PEDOT:F spectrum, the peaks associated with the sulfonate moieties exhibit slight shifts of varying degrees, suggesting the presence of electrostatic interaction between SO_3^- and PEDOT.

To demonstrate the contribution of PEDOT to electronic conduction, the density of states (DOS) of PFSA and PEDOT:F was calculated using DFT [49,50]. The DOS of the PFSA and PEDOT:F is presented in Fig. 2c. In comparison to PEDOT:F, the forbidden bandwidth between the highest occupied molecular orbital (HOMO) and the lowest unoccupied molecular orbital (LUMO) of PFSA is wider, and the linear region lacks free electrons, resulting in diminished electrical conductivity. In contrast, PEDOT:F exhibits superior conductivity compared to PFSA, with an absence of linear regions. Furthermore, the density of additional states at the Fermi energy level of PEDOT:F undergoes augmentation, indicating an enhancement in electronic conductivity with the incorporation of PEDOT. To delve deeper into the influence of varied PEDOT ratios on conductivity, the electronic conductivity of the Membrane-Integrated Polymer Electrolyte Composite (MPEC) PEDOT:F was gauged using AC impedance in conjunction with a blocking electrode (see Fig. S2). Fig. 2d summarizes the obtained results, demonstrating a direct proportionality between electronic conductivity and the ratio of PEDOT, consistent with the DOS analysis.

The CL constitutes a hierarchical structure wherein electrochemical reactions, charge transfer, and mass transport transpire concurrently upon satisfaction of triple-phase boundaries conditions [51]. The microstructure and dispersion characteristics of the ionomer play a pivotal role in shaping the three-phase boundaries, formed through its interaction with the catalyst, as well as the network structure of the CL. These factors, in turn, significantly influence the performance of the electrolytic reaction in PEMWE [36,52]. Consequently, the microstructural alterations of various PEDOT:F compositions were scrutinized through Small-Angle X-ray Scattering (SAXS). Fig. 2e delineates the plots

(a)

(b)
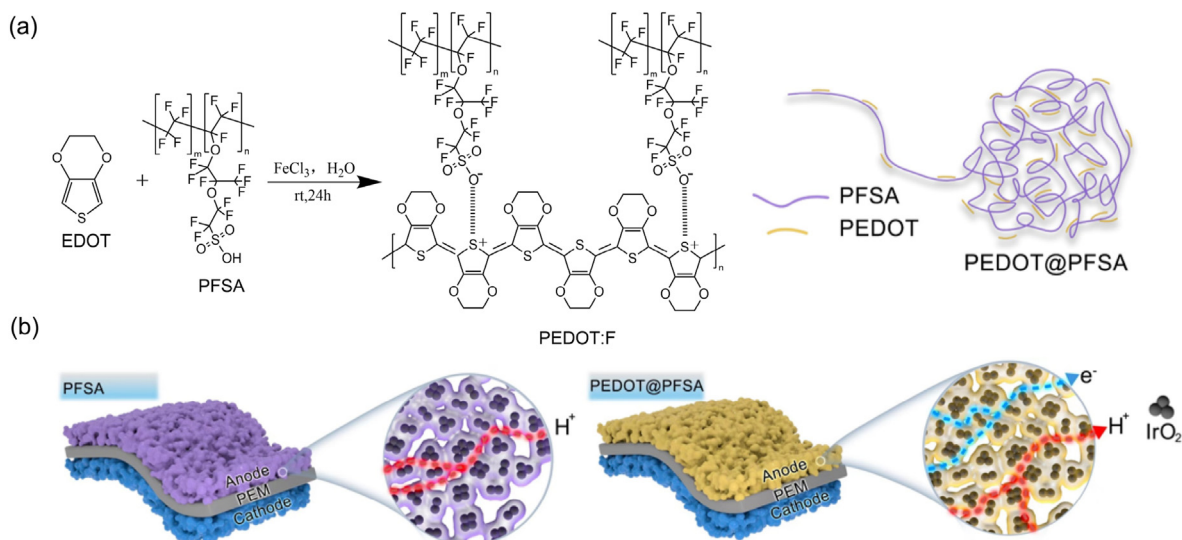
Fig. 1. (a) The reaction route to synthesize the PEDOT:PFSA; (b) The schematics of the MEA with PEDOT:F and conventional Nafion (PFSA) as catalyst binders.

of intensity versus the q value for different ratios of PEDOT:F. As the proportion of PFSA increases, the peak position of the scattering vector q also increases. Employing the Bragg spacing relation, $d=2\pi q^{-1}$, where d signifies the associated length and q represents the scattering vector, it can be inferred that the stacking between PEDOT and PFSA in dispersions with a higher percentage of PFSA is denser, resulting in shorter spacing [53]. The two-dimensional (2D) SAXS scattering images corroborate this variation (see Fig. 2g–k). Although the peak position of the scattering vector q increases with the PFSA fraction, this trend is less pronounced for the last three fractions of PEDOT:F. Additionally, for PFSA ionomers, the peak position of the scattering vector q shifts toward lower q values with increasing humidity. A lower q value or a larger spacing d indicates the presence of larger ionic clusters, thus favoring water adsorption [54]. In comparison, PEDOT:F-1 exhibits the lowest scattering peak position and the largest spacing, fostering the extension of the PFSA side chain structure. With more abundant hydrophilic groups, this composition facilitates the formation of larger hydrophilic ion clusters, thereby contributing to a more favorable network formation in the CL. This, in turn, enhances reactant water adsorption on the catalyst surface and augments proton-electron conduction.

The OER performances of commercial IrO_2 with prepared PEDOT:F samples were assessed in 0.1 M $HClO_4$, with PFSA included for comparison [55,56]. Fig. 3a–b depict the LSV curves and the corresponding overpotentials of PEDOT:F and D520 as binders, respectively. A smaller overpotential indicates a faster progression of the electrochemical reaction, and the OER performance of the five different ratios of PEDOT:F surpasses that of D520 as the binder. As inferred from Fig. 2d, the electronic conductivity of PEDOT:F decreases with the reduction in the percentage of PEDOT. The LSV curves and the corresponding overpotentials illustrated in Fig. 3a–b also exhibit a concurrent change, wherein the LSV performance deteriorates with the decrease in the percentage of PEDOT, resulting in increased overpotentials. Notably, PEDOT:F-1, which possesses the highest electronic conductivity, demonstrates a reduction of 14 mV in overpotential compared to D520. Supplementary Fig. S3 illustrates the corresponding Tafel slopes, revealing that all ratios of PEDOT:F have lower Tafel slope values than D520. Fig. 3c presents a comparison of the double-layer capacitance (Cdl) values of different binders. Calculating Cdl enables the derivation of its corresponding electrochemical active surface area (ECSA) [57]. ECSA is positively correlated with Cdl, and a larger Cdl value indicates more exposure to the active site and, consequently, greater electrocatalytic activity. Cdl values were obtained by cycling the potential in the range of 1.00–1.10 V at different sweep rates, and in this study, the sweeping

speeds were 20, 40, 60, 80, and 100 mV/s. Additionally, the corresponding Cyclic Voltammetry (CV) profiles are shown in Supplementary Fig. S4. From Fig. 3c, it is evident that the Cdl value of PEDOT:F is greater than that of D520 as the binder, suggesting superior electrocatalytic activity after incorporating PEDOT:F as the binder. Furthermore, the Cdl values of different ratios increase with the rise in the proportion of PEDOT. Fig. 3d displays the Nyquist plots of electrochemical impedance spectra measured under 10 mA cm^{-2}. In accordance with the preceding results, PEDOT:F exhibits a smaller charge transfer resistance (Rct) compared to D520, signifying a faster charge transfer rate with the inclusion of PEDOT:F. Combining the DOS and SAXS results in Fig. 2c and e, the superior performance of PEDOT:F-1 can be attributed to the enhanced electrical conductivity introduced by PEDOT relative to PFSA. Additionally, the larger hydrophilic ionic clusters in PEDOT:F-1 facilitate the absorption of reactant water on the catalyst surface, thereby enhancing proton conduction and promoting the electrochemical reaction. For Rotating Disk Electrode (RDE), although the Nafion ionomer can prevent catalyst detachment and ensure stability, its electronic insulating property detrimentally affects electrochemical performance to a certain extent. The addition of PEDOT improves electronic conductivity, resulting in a notable enhancement in the electrochemical performance of the RDE disk electrode.

The role of PEDOT on catalytic activity was investigated by DFT calculations [49,58]. The detailed method is presented in the Supporting Information. OER is a four-proton coupled electron transfer reaction in which the conventional adsorbate evolution mechanism (AEM) is employed in this work. The OER reaction mechanism of PFSA-IrO_2 and PEDOT:F–IrO_2 are shown in Fig. 4a. Fig. 4b demonstrates the OER free energies of PEDOT:F–IrO_2 and PFSA-IrO_2, where the rate-determining step (RDS) is * OOH formation for both PEDOT:F–IrO_2 and PFSA-IrO_2, and thus the catalytic activity of OER can be evaluated in terms of the value Z ($\Delta G(*OOH)-\Delta G(*O)$) [59,60]. The calculated Z value of 2.19 eV for PEDOT:F–IrO_2 is lower than that of 2.27 eV for PFSA-IrO_2, and the decrease of Z in PEDOT:F–IrO_2 can be ascribed to the decrease of adsorption energy of *OOH on the surface of PEDOT:F–IrO_2, suggesting that the incorporation of PEDOT can diminish the energy barrier of OER and thus improve the catalytic activity of OER, which coincides with the experimental results. Combined with the DOS calculations, it is speculated that the incorporation of PEDOT improves the electrical conductivity and the active site area, which results in the catalytic activity of the OER.

To investigate the proton conduction of MPEC, proton resistance measurements were conducted on catalyst layers employing different
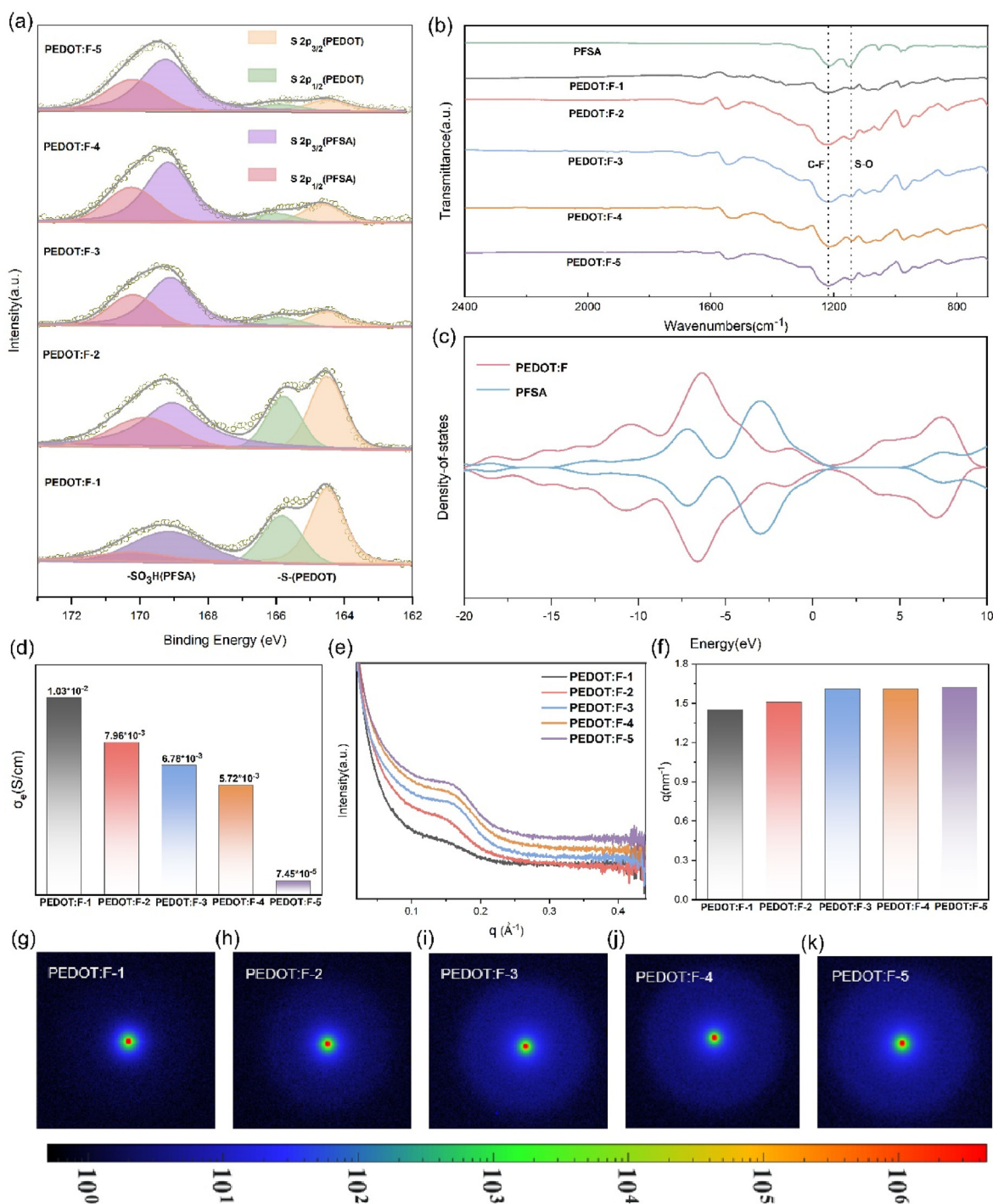
Fig. 2. (a) XPS spectra of PEDOT:F; (b) FTIR spectra of PEDOT:F and PFSA; (c) The density of states (DOS) of the PFSA and PEDOT:F; (d) The electronic conductivity of different ratios of PEDOT:F at room temperature; (e) Plots of intensity versus the q value of different ratios of PEDOT:F; (f) The q values at the scattering peaks of different ratios of PEDOT:F; (g–k) 2D SAXS patterns of different ratios of PEDOT:F.

binders. The four-probe test method was employed at 80 °C and 100 % Relative Humidity (RH), mirroring the conditions for single-cell testing. The transport of electrons was isolated by incorporating proton exchange membranes on both sides of the catalyst layers, as illustrated in Fig. S2. As depicted in Fig. S5a, the resistance of PEDOT:F decreases with the increase in the percentage of PFSA for various ratios of PEDOT:F. Notably, the proton resistance of PEDOT:F-3 exhibits minimal deviation compared to that of D520. In comparison to the cathode catalyst layer (CCL) employing Pt/C as the catalyst, the sheet resistance of the anode CL is significantly higher, limiting the utilization efficiency of PEMWE. To

elucidate the impact of introducing MPEC binder on CL resistance, the sheet resistance of the anode CL was measured (see Fig. S5b). The findings indicate that all the sheet resistances of CL experienced a descent to a certain degree after the addition of MPEC as the binder in comparison to D520.

Fig. 5a–d shows the TEM images of anode CLs prepared by different ratios of PEDOT:F and D520. It can be seen that the distribution of catalysts in the CLs prepared with PEDOT:F appears more homogeneous, while the CLs prepared with D520 exhibit a heterogeneous distribution with more noticeable agglomerates. Additionally, the cross-sectional
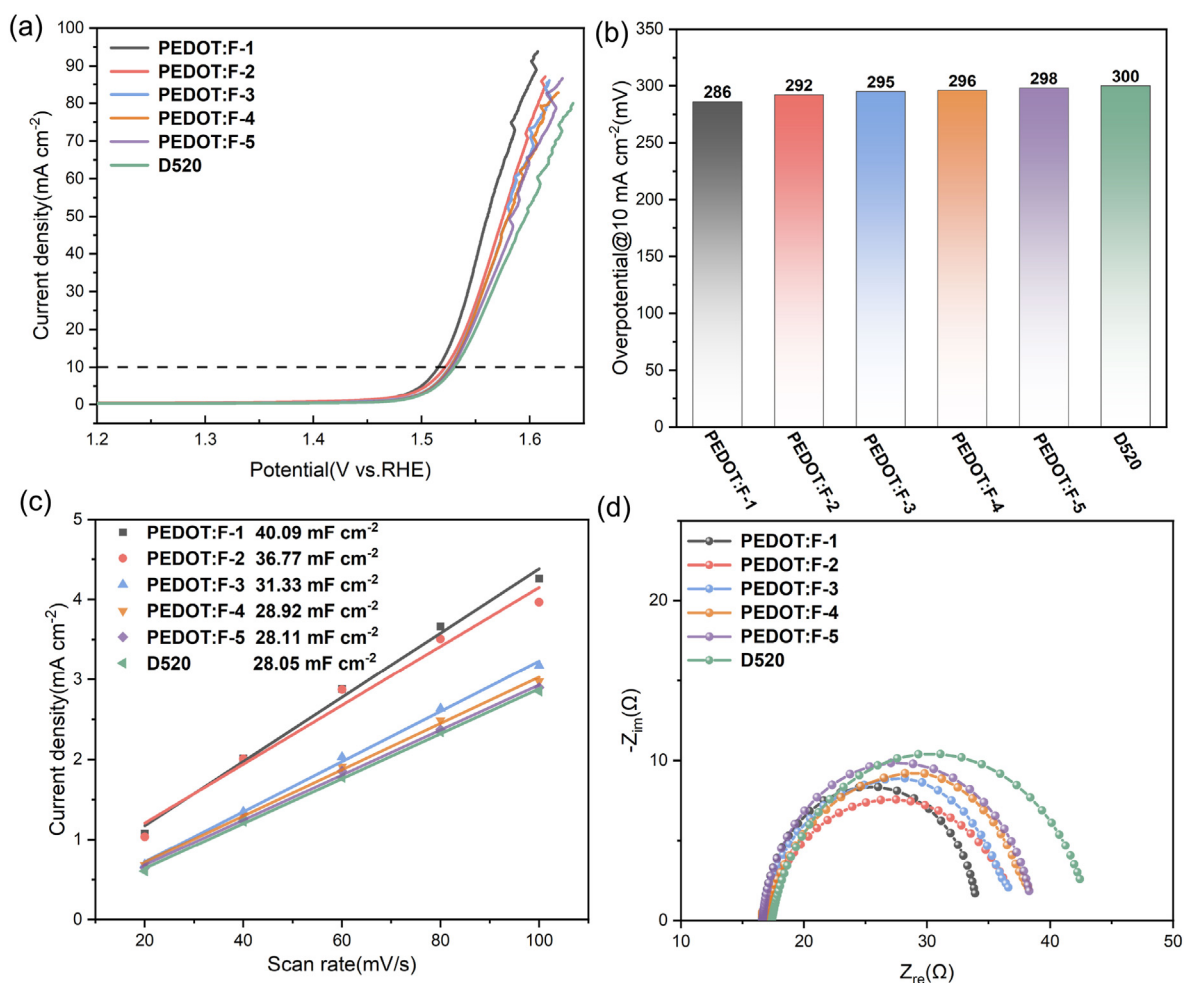
Fig. 3. Electrochemical OER performances of PEDOT:F and PFSA. (a) LSV curves; (b) Overpotential @10 mA cm^{-2}; (c) Double-layer capacitance (Cdl) at different sweep rates; (d) Nyquist plots of electrochemical impedance spectra measured under 10 mA cm^{-2} of different ratios of PEDOT:F and D520 as binders.

micrographs of anode CLs as prepared with the various ratios of PEDOT:F and D520 are shown in Fig. 5e–h. Consistent with the TEM observations, the CL prepared with D520 displays a highly inhomogeneous distribution, and the pore structure is more evident compared to the other three CLs. The zeta potential measurements (See Fig. 5i) reveal that the addition of PEDOT:F increases the zeta potential value of the catalyst inks. It is presumed that PEDOT:F acts as a dispersant, contributing to ink stability and reduced agglomeration after its addition. Increased agglomeration tends to augment the pore volume of macroporous pores, which is unfavorable for the generation of active catalytic sites [61]. To further analyze the effect of PEDOT:F on pore structure, the MIP test was employed to assess the pore structure of these CLs. Fig. 5j–k illustrate the pore size distribution of different CLs, categorized into primary pores, secondary pores, and macropores, with corresponding pore size ranges of <20 nm, 20–1000 nm, and >1000 nm, respectively. The remaining three CLs, prepared with PEDOT:F, exhibit fewer macropores and more primary pores compared to the CL prepared with D520. These findings suggest that the addition of PEDOT:F contributes to the reduction of agglomerates, fostering the formation of a more homogeneous CL. This is conducive to improving catalyst utilization and constructing more catalytically active sites for OER.

The electrochemical performance of the electrolyzer was evaluated to elucidate the electrolytic efficiency of applying PEDOT:F to the electrodes. Polarization curves of MEA prepared with different samples and the corresponding voltages at different current densities are presented in Fig. 6a. MEAs prepared using PEDOT:F-1 and PEDOT:F-2 exhibit significantly better performance than D520. Interestingly, despite the RDE test

showing a correlation between electronic conductivity and performance, the MEA performance does not strictly follow this trend. The best performance was observed in the group of PEDOT:F-2, achieving a superior performance of 1.713 V at 2 A cm^{-2}. This inconsistency suggests that focusing solely on electronic conductivity may not be the sole factor in enhancing MEA performance; a compromise between electronic and proton conductivity appears to be crucial. As displayed in Fig. 6a, the MEA performance of both PEDOT:F-1 and PEDOT:F-3 is inferior to that of PEDOT:F-2. Hence, achieving the optimal electrochemical performance in proton exchange membrane water electrolysis (PEMWE) single-cells requires a balanced consideration of both electronic and proton conductivity. Tafel slopes and OER overpotentials of MEA prepared by different binders were obtained to evaluate catalytic activity (Fig. S6). The Tafel slope and OER overpotential of MEA prepared with PEDOT:F are lower than that of D520, with PEDOT:F-2 exhibiting the lowest values., which is consistent with the polarization curves and DFT results. The introduction of MPEC is believed to better align with the triple-phase boundaries theory, enhance the active site area, and ultimately lead to improved catalytic activity. EIS impedance tests were performed for different MEAs at low and high current densities, and the data were fitted to impedance plots using equivalent circuit diagrams. The corresponding Nyquist plots and resistance values are displayed in Fig. 6b–c. MEA performance is influenced by both ohmic and mass transfer resistance. The comparison shows that the resistance of PEDOT:F-2 exhibits a minimum at both high and low current densities, reflecting the lowest voltage values and the best performance among all the samples. Stability is a crucial consideration for practical application in PEMWE. To assess
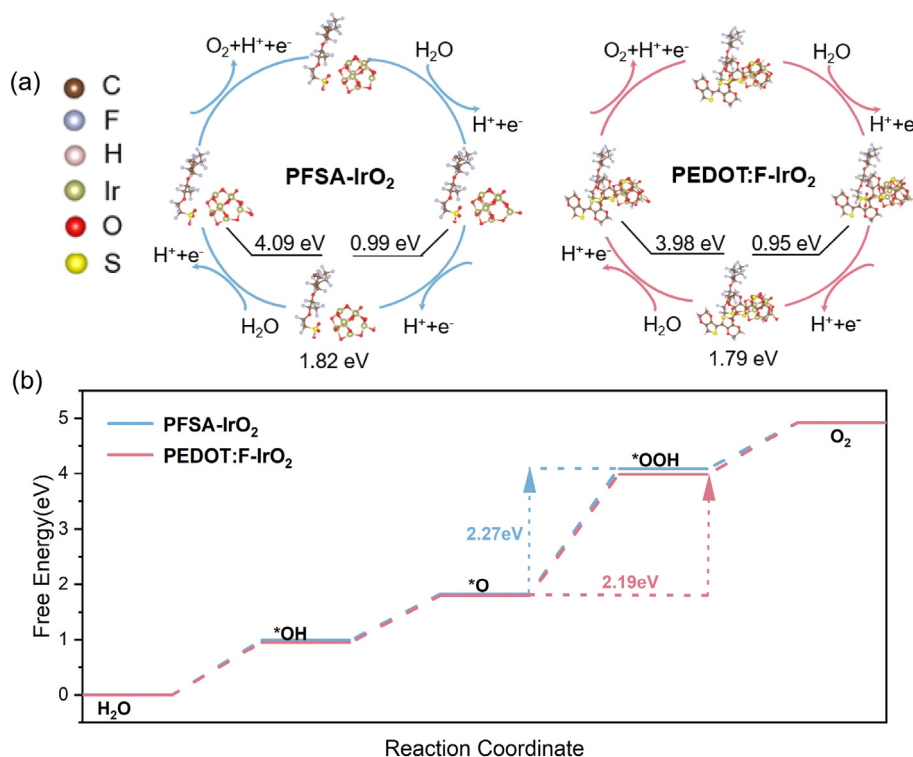
Fig. 4. (a) OER reaction mechanism of PFSA-IrO$_2$ and PEDOT:F–IrO$_2$; (b) Calculated OER free-energy diagrams for PFSA-IrO$_2$ and PEDOT:F–IrO$_2$.

the stability of the homemade binder, the MEA prepared with PEDOT:F-2, exhibiting the best performance, was selected for the stability test. The results in Fig. 6d demonstrate that the voltage of the MEA prepared with the homemade binder remains stable and virtually unchanged during the test time. The observed increase in voltage by only 0.007V indicates that the MEA with the homemade binder maintains good stability during operation.

3. Conclusions

In conclusion, we synthesized a mixed electronic and proton conductor, PEDOT:F, designed to facilitate the conduction of electrons and protons, respectively. This dual conduction property contributes to rapid electron transport and enhances catalytic activity by increasing the active surface area for OER. The synthesized samples underwent qualification through various analyses, including FTIR spectroscopy, XPS, and SAXS tests. Conductivity measurements of both the samples and the CL were conducted by fabricating blocking electrodes. The sheet resistance measurements of CL revealed that the application of MPEC could ameliorate the poor conductivity of CL. Moreover, MIP, zeta potential, TEM, and SEM results demonstrate that PEDOT improves the stability and dispersion of the catalyst ink. The resulting membrane-integrated electrochemical cell (MIEC) was employed in OER reactions and PEMWE single-cell tests. The outcomes indicate that, for RDE, the introduction of PEDOT enhances electronic conductivity, thereby reducing mass transfer resistance and further amplifying the electrocatalytic activity of the OER reaction. DFT results aligns with the experimental findings, affirming that the inclusion of PEDOT heightens catalytic activity by augmenting electronic conductivity and lowering the energy barrier. In the cell test, the MEA prepared with PEDOT:F-2 exhibits superior performance, achieving 1.713 V at 2 A cm^{-2}. In the context of the full-cell reaction, a balanced consideration of both electronic and proton conductivity proves advantageous for overall performance improvement. The stability test demonstrates that the MEA prepared with PEDOT:F exhibits robust durability, meeting the requirements for practical PEMWE applications.

4. Experimental section

4.1. Materials

3,4-Ethylenedioxythiophene (EDOT, 99 %) and FeCl$_3$ were obtained by Aladdin. PFSA ionomer(Nafion D520 dispersion)with a short side chain (5 wt% in H$_2$O, equivalent weight (eq. wt of 1000) was adopted as the counterions and was purchased from Dupont. The IrO$_2$ catalyst was purchased from KAIDA, the Pt/C catalyst was obtained from TANAKA.

4.2. Synthesis of PEDOT:F

The PEDOT:F was synthesized by oxidative chemical polymerization. Firstly, the solid content of D520 ionomer dispersion, also known as PFSA ionomer dispersion, was changed from 5 % to 10 %. Subsequently, PFSA ionomer dispersion (2 g,10 wt% in H$_2$O, eq. wt 1100) and EDOT (0.2 g) were mixed in 20 ml DI water and stirred vigorously for 2 h to form an emulsion. Following this, FeCl$_3$ (0.13 g) was introduced in 4 ml of DI water as the oxidant. Stirring continued for 24 h after the addition of the oxidizing agent, the obtained dispersions were purified through a semi-permeable membrane (500 Da) to eliminate unreacted material, and then the purified aqueous dispersion was centrifuged. The products after centrifugation were dispersed in 2-propanol (IPA) and sonicated using an ultrasonic cell crusher for 2 h to form alcohol dispersions. Different ratios of PEDOT:F were obtained by varying the ratio of EDOT and PFSA. The obtained samples were denoted as PEDOT:F-1, PEDOT:F-2, PEDOT:F-3, PEDOT:F-4, and PEDOT:F-5 with progressively increasing percentages of PFSA.

4.3. Physical characterization

The materials were characterized using Fourier transform infrared spectroscopy (FTIR, Nicolet Magna 6700). The thermal stability of the composites was measured on a thermogravimetric analyzer (STA 449 F3 Jupiter). X-ray photoelectron spectroscopy characterization was performed with an AXIS SUPRA instrument. The morphology and
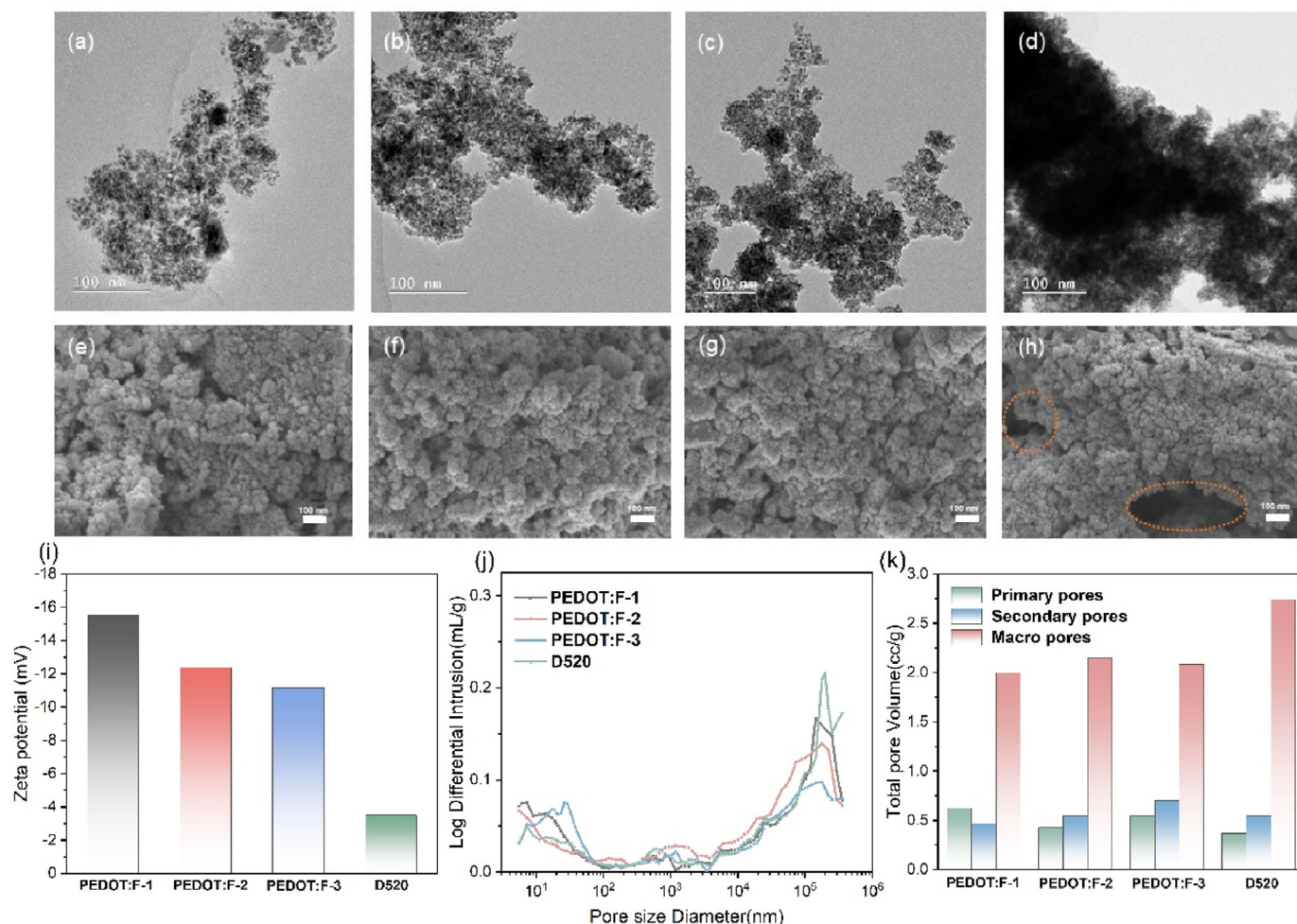
Fig. 5. TEM images of CLs: (a) PEDOT:F-1, (b) PEDOT:F-2, (c) PEDOT:F-3, (d) D520; SEM images of CLs: (e) PEDOT:F-1, (f) PEDOT:F-2, (g) PEDOT:F-3, (h) D520; (i) The Zeta potential of catalyst inks prepared by different binders; (j) Pore size distribution of CLs with different binders; (k) Variation of total pore volume for different CL.

distribution of the catalysts was analyzed using scanning electron microscopy (SEM, Zeiss Ultra Plus) and transmission electron microscopy (TEM, JEM-F200). The prepared dispersions were analyzed through small-angle X-ray scattering (SAXS) using X-rays at a wavelength of 1.54 Å on a SAXS device (Xeuss 3.0 SAXS/WAXS). Mercury intrusion porosimetry (MIP, AutoPore V 9600) was used to identify the pore size distribution in CL. For zeta potential analysis, the diluted catalyst ink was measured with the 90Plus Zeta.

Measurement of the electronic conductivity of materials by the method of blocking electrodes combined with AC impedance. Stainless steel was used as the ion-blocking and electron-conducting material, and the composite material was pressed and compacted in the powder under the pressure of 12 MPa [62]. The proton resistance was measured by sandwiching the proton exchange membrane on two sides of the CL to isolate the passage of electrons, and measured by the four-probe method combined with the AC impedance method [63,64]. The sheet resistance of CLs with different binders was measured using a four-point probe meter (ST2253) [39].

4.4. MEA preparation

The preparation of Membrane electrode assemblies were prepared using catalyst-coated membrane (CCM) approach [65]. IrO$_2$, DI water, isopropanol, and the ionomer dispersion solution were mixed to control the solid content of 18 % and the ratio of ionomer to catalyst was 1/9

(I/catalyst=1/9). The catalyst ink was ultrasonically dispersed in an ice bath condition in an Ultrasonic Cell Crusher, after which it was transferred for ball milling. The catalyst for the cathode was 50 wt% Pt/C with the solid content controlled at 8 %, and the mass ratio of ionomer to catalyst was 0.8 (I/catalyst=0.8), with the remaining steps identical to the anode catalyst ink preparation steps described above. The use of polytetrafluoroethylene as the substrate for coating catalyst inks and the CL of 4 × 4 cm^2 was obtained after drying. The IrO$_2$ loading of the anode CL was controlled to be 1.6 ± 0.15 mg cm^{-2}, and the Pt loading of the cathode was kept to 0.4 ± 0.05 mg cm^{-2}. The cathode and anode CLs are being transferred to both sides of the N212 proton exchange membranes by hot pressing.

4.5. Electrochemical measurements

The OER activity of the electrochemical catalyst was tested on the electrochemical workstation (CHI 660 E). The potentials described in the work have been normalized to reversible hydrogen electrodes and the electrolyte used was 0.1 M HClO$_4$ aqueous solution. The working electrode was a glassy carbon electrode of 0.5 cm diameter, with a platinum electrode and a saturated calomel electrode acting as the counter and reference electrode. 10 μL of the prepared catalyst ink was dispensed with a pipette gun and applied uniformly on the glassy carbon electrode. Before electrochemical measurements, activation was performed by cyclic voltammetry (CV) under the conditions of a sweep range of 0–1.2 V, a
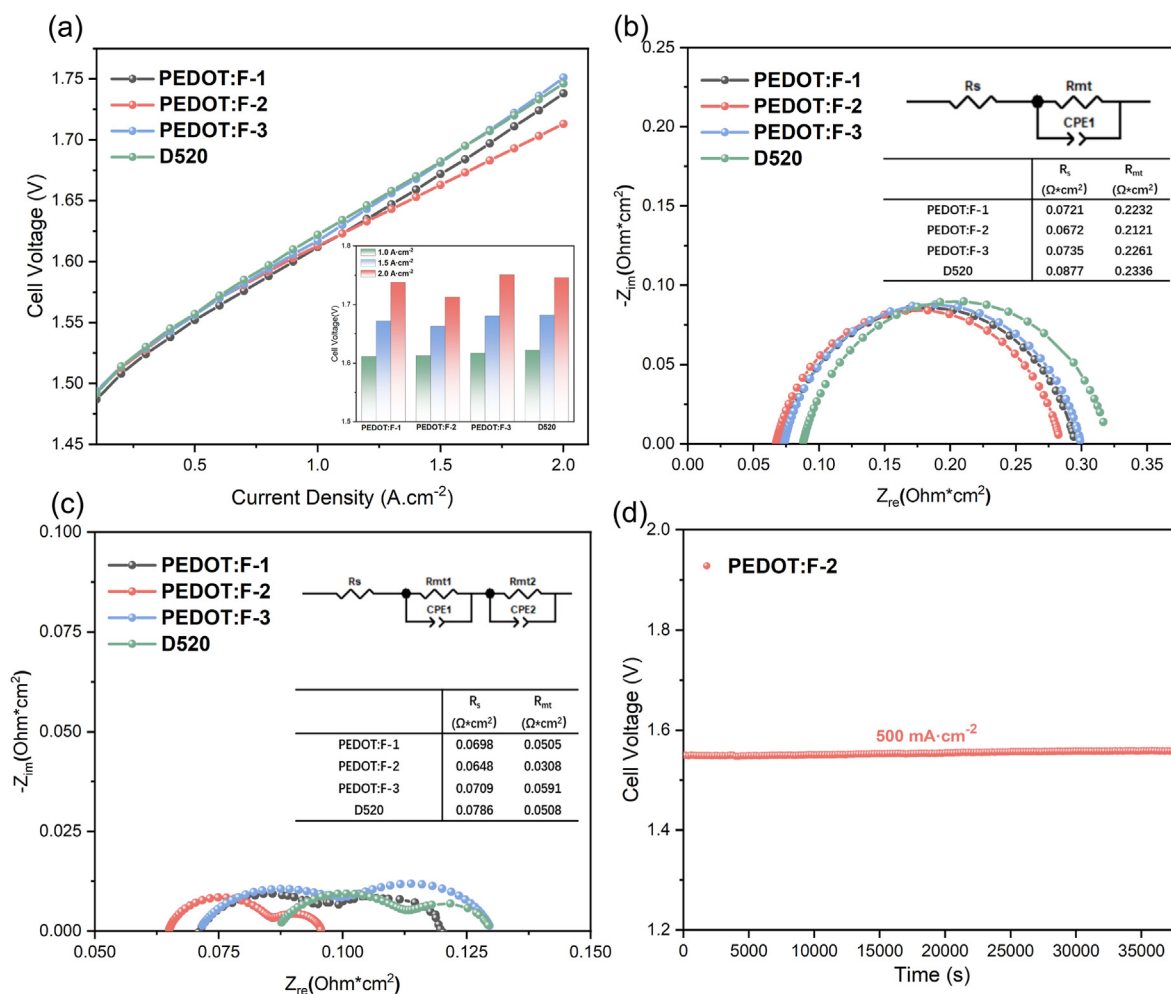
Fig. 6. Electrochemical performances of different binders in PEMWE. (a) Polarization curves; (b) Nyquist plots at 0.1 A cm^{-2}; (c) Nyquist plots at 1.5 A cm^{-2}; (d) Durability test of MEA with PEDOT:F.

sweep rate of 50 mV/s, and 40 cycles. Linear sweep voltammetry (LSV) was operated with a holding speed of 1600 rpm, a sweep range of 1.2–1.9 V, and a sweep rate of 5 mV/s. Electrochemical impedance spectroscopy (EIS) was measured at the voltage corresponding to 10 mA cm^2 with a frequency of 0.1–10 kHz. The CV test was performed at a voltage of 1–1.1 V with a sweep rate from 20 mV to 100 mV, increasing the sweep rate by 20 mV each time to obtain the double-layer capacitance.

The electrochemical workstation used for single-cell measurements was Kolibrik PTC-05100E. The membrane electrode assemblies were activated before the tests. The activation was carried out at 1.6 V and waited for its corresponding current to stabilize for 2 h to complete the activation. A steady-state polarization test was used to obtain the polarization curve, the test range was 0.1 A cm^{-2}-2 A cm^{-2}. Similarly, the current density is stabilized for 5 min for each 100 mA cm^{-2} increase in current density, and then the steady state voltage value at that current density is taken. The amplitude of the perturbation imposed by the EIS test was 5 %, and the frequency range was 0.1–10 kHz. All of the above tests were conducted under pure water conditions, with the inlet water temperature maintained at 80 °C and the water flow rate at 40 ml min^{-1}.

Declaration of competing interest

The authors declare that they have no known competing financial interests or personal relationships that could have appeared to influence the work reported in this paper.

Acknowledgments

Appendix A. Supplementary data

Supplementary data to this article can be found online at https://doi.org/10.1016/j.apmate.2024.100203.

References

[1] G. Cipriani, V. Di Dio, F. Genduso, D. La Cascia, R. Liga, R. Miceli, G. Ricco Galluzzo, Perspective on hydrogen energy carrier and its automotive applications, Int. J. Hydrogen Energy 39 (16) (2014) 8482–8494.

[2] X. Li, L. Zhao, J. Yu, X. Liu, X. Zhang, H. Liu, W. Zhou, Water splitting: from electrode to green energy system, Nano-Micro Lett. 12 (2020) 131.

[3] T. Wang, X. Cao, L. Jiao, PEM water electrolysis for hydrogen production: fundamentals, advances, and prospects, Carbon Neutrality 1 (2022) 21.

[4] Z. Yu, C. Si, F.J. Escobar-Bedia, A.P. LaGrow, J. Xu, M.J. Sabater, I. Amorim, A. Araujo, J.P.S. Sousa, L. Meng, J.L. Faria, P. Concepcion, B. Li, L. Liu, Bifunctional atomically dispersed ruthenium electrocatalysts for efficient bipolar membrane water electrolysis, Inorg. Chem. Front. 9 (2022) 4142–4150.

[5] P.K. Giesbrecht, A.M. Müller, C.G. Read, S. Holdcroft, N.S. Lewis, M.S. Freund, Vapor-fed electrolysis of water using earth-abundant catalysts in Nafion or in

bipolar nafion/poly(benzimidazolium) membranes, Sustain. Energy Fuels 3 (2019) 3611–3626.

[6] B. Mayerhöfer, D. McLaughlin, T. Böhm, M. Hegelheimer, D. Seeberger, S. Thiele, Bipolar membrane electrode assemblies for water electrolysis, ACS Appl. Energy Mater. 3 (2020) 9635–9644.

[7] Y. Ding, P. Cai, Z. Wen, Electrochemical neutralization energy: from concept to devices, Chem. Soc. Rev. 50 (2021) 1495–1511.

[8] Q. Li, A. Molina Villarino, C.R. Peltier, A.J. Macbeth, Y. Yang, M.J. Kim, Z. Shi, M.R. Krumov, C. Lei, G.G. Rodríguez-Calero, J. Soto, S.H. Yu, P.F. Mutolo, L. Xiao, L. Zhuang, D.A. Muller, G.W. Coates, P. Zelenay, H.D. Abruña, Anion exchange membrane water electrolysis: the future of green hydrogen, J. Phys. Chem. C 127 (2023) 7901–7912.

[9] D.S. Falcão, Green hydrogen production by anion exchange membrane water electrolysis: status and future perspectives, Energies 16 (2) (2023) 943.

[10] J. Ren, J. Xu, M. Ju, X. Chen, P. Zhao, L. Meng, J. Lei, Z. Wang, Long-term durable anion exchange membranes based on imidazole-functionalized poly(ether ether ketone) incorporating cationic metal–organic framework, Adv. Powder Mater. 1 (2) (2022) 100017.

[11] Q. Feng, X.Z. Yuan, G. Liu, B. Wei, Z. Zhang, H. Li, H. Wang, A review of proton exchange membrane water electrolysis on degradation mechanisms and mitigation strategies, J. Power Sources 366 (2017) 33–55.

[12] K. Bareiß, C. de la Rua, M. Möckl, T. Hamacher, Life cycle assessment of hydrogen from proton exchange membrane water electrolysis in future energy systems, Appl. Energy 237 (2019) 862–872.

[13] H. Jiang, R. Luo, Y. Li, W. Chen, Recent advances in solid–liquid–gas three-phase interfaces in electrocatalysis for energy conversion and storage, EcoMat 4 (4) (2022) E12199.

[14] Y. Zhu, W. Zhou, Y. Zhong, Y. Bu, X. Chen, Q. Zhong, M. Liu, Z. Shao, A perovskite nanorod as bifunctional electrocatalyst for overall water splitting, Adv. Energy Mater. 7 (8) (2017) 1602122.

[15] Y. Tong, P. Chen, T. Zhou, K. Xu, W. Chu, C. Wu, Y. Xie, A bifunctional hybrid electrocatalyst for oxygen reduction and evolution: cobalt oxide nanoparticles strongly coupled to B,N-decorated graphene, Angew. Chem. Int. Ed. 56 (25) (2017) 7121–7125.

[16] J. Bai, L. Cheng, S. Liu, H. Zhang, Y. Lian, Y. Deng, Q. Zhou, Y. Tang, Y. Su, Unravel the mechanism of d-orbital modulation and oxygen vacancy in cerium-doped RuO2 catalysts for acidic oxygen evolution reaction, Appl. Surf. Sci. 642 (2024) 158613.

[17] Z. Li, X. Wu, X. Jiang, B. Shen, Z. Teng, D. Sun, G. Fu, Y. Tang, Surface carbon layer controllable Ni3Fe particles confined in hierarchical N-doped carbon framework boosting oxygen evolution reaction, Adv. Powder Mater. 1 (2) (2022) 100020.

[18] H. Jing, P. Zhu, X. Zheng, Z. Zhang, D. Wang, Y. Li, Theory-oriented screening and discovery of advanced energy transformation materials in electrocatalysis, Adv. Powder Mater. 1 (1) (2022) 100013.

[19] J. Mo, Z. Kang, S.T. Retterer, D.A. Cullen, T.J. Toops, J.B. Green, M.M. Mench, F.Y. Zhang, Discovery of true electrochemical reactions for ultrahigh catalyst mass activity in water splitting, Sci. Adv. 2 (11) (2016) e1600690.

[20] R. Cheng, Y. Min, H. Li, C. Fu, Electronic structure regulation in the design of low-cost efficient electrocatalysts: from theory to applications, Nano Energy 115 (2023) 108718.

[21] G. Yang, S. Yu, Z. Kang, Y. Li, G. Bender, B.S. Pivovar, J.B. Green, D.A. Cullen, F.Y. Zhang, Building electron/proton nanohighways for full utilization of water splitting catalysts, Adv. Energy Mater. 10 (16) (2020) 1903871.

[22] J. Luo, X. Wang, Y. Gu, D. Wang, S. Wang, W. Li, Y. Zhou, J. Zhang, Constructing hollow nanocages of Co3O4-CoMoO4 heterostructure for efficient electrocatalytic oxygen evolution reaction, Appl. Surf. Sci. 606 (2022) 154562.

[23] M. Huang, L. Fan, Y. Jin, Y. Niu, X. Bai, S. Xu, J. Fan, H. Li, Systematic study of oxygen evolution reaction activity and stability of SnnSbmNbIOx ternary oxide-supported IrO2 catalysts, ACS Appl. Energy Mater. 6 (12) (2023) 6456–6466.

[24] M. Gollasch, J. Schmeling, C. Harms, M. Wark, Comparative analysis of synthesis routes for antimony-doped tin oxide-supported iridium and iridium oxide catalysts for OER in PEM water electrolysis, Adv. Mater. Interfac. 10 (15) (2023) 2300036.

[25] V. Chabot, D. Higgins, A. Yu, X. Xiao, Z. Chen, J. Zhang, A review of graphene and graphene oxide sponge: material synthesis and applications to energy and the environment, Energy Environ. Sci. 7 (2014) 1564–1596.

[26] M. Zhao, Y. Wang, Q. Ma, Y. Huang, X. Zhang, J. Ping, Z. Zhang, Q. Lu, Y. Yu, H. Xu, Y. Zhao, H. Zhang, Ultrathin 2D metal-organic framework nanosheets, Adv. Mater. 27 (45) (2015) 7372–7378.

[27] C. Rozain, E. Mayousse, N. Guillet, P. Millet, Influence of iridium oxide loadings on the performance of PEM water electrolysis cells: part II – advanced oxygen electrodes, Appl. Catal., B 182 (2016) 123–131.

[28] I. Ali Khan, P. Morgen, S. Gyergyek, R. Sharma, S. Ma Andersen, Reduced valence state of iridium supported on antimony doped tin oxide as a highly active and robust oxygen evolution reaction electrocatalyst for proton exchange membrane-based electrolysis, Appl. Surf. Sci. 646 (2024) 158924.

[29] G. Yang, W. Wang, Z. Xie, S. Yu, Y. Li, L. Ding, K. Li, F.Y. Zhang, Favorable morphology and electronic conductivity of functional sublayers for highly efficient water splitting electrodes, J. Energy Storage 36 (2021) 102342.

[30] J. Tang, Y. Zhong, C. Su, Z. Shao, Silver compositing boosts water electrolysis activity and durability of RuO2 in a proton-exchange-membrane water electrolyzer, Small Science 3 (9) (2023) 2300055.

[31] G. Yang, S. Yu, Y. Li, K. Li, L. Ding, Z. Xie, W. Wang, F.Y. Zhang, Role of electron pathway in dimensionally increasing water splitting reaction sites in liquid electrolytes, Electrochim. Acta 362 (2020) 137113.

[32] S. Higashi, A. Beniya, Ultralight conductive IrO2 nanostructured textile enables highly efficient hydrogen and oxygen evolution reaction: importance of catalyst layer sheet resistance, Appl. Catal., B 321 (2023) 122030.

[33] E. Antolini, E.R. Gonzalez, Polymer supports for low-temperature fuel cell catalysts, APPL CATAL A-GEN 365 (1) (2009) 1–19.

[34] W. Xu, K. Scott, The effects of ionomer content on PEM water electrolyser membrane electrode assembly performance, Int. J. Hydrogen Energy 35 (21) (2010) 12029–12037.

[35] M. Bernt, H.A. Gasteiger, Influence of ionomer content in IrO2/TiO2 electrodes on PEM water electrolyzer performance, J. Electrochem. Soc. 163 (2016) F3179–F3189.

[36] A. Zhang, G. Zhu, M. Zhai, S. Zhao, L. Zhu, D. Ye, Y. Xiang, T. Tian, H. Tang, Construction of catalyst layer network structure for proton exchange membrane fuel cell derived from polymeric dispersion, J. Colloid Interface Sci. 638 (2023) 184–192.

[37] S. Zhao, R. Wang, T. Tian, H. Liu, H. Zhang, H. Tang, Self-assembly-cooperating in situ construction of MXene–CeO2 as hybrid membrane coating for durable and high-performance proton exchange membrane fuel cell, ACS Sustain.Chem. Eng. 10 (13) (2022) 4269–4278.

[38] C.V. Pham, D. Escalera-López, K. Mayrhofer, S. Cherevko, S. Thiele, Essentials of high performance water electrolyzers – from catalyst layer materials to electrode engineering, Adv. Energy Mater. 11 (44) (2021) 2101998.

[39] J. Mo, G. Yang, Y. Li, Z. Kang, G. Bender, B.S. Pivovar, J.B. Green, F.Y. Zhang, Experimental studies on the effects of sheet resistance and wettability of catalyst layer on electro-catalytic activities for oxygen evolution reaction in proton exchange membrane electrolysis cells, Int. J. Hydrogen Energy 45 (51) (2020) 26595–26603.

[40] H. Liu, D. Zhao, M. Dai, X. Zhu, F. Qu, A. Umar, X. Wu, PEDOT decorated CoNi2S4 nanosheets electrode as bifunctional electrocatalyst for enhanced electrocatalysis, Chem. Eng. J. 428 (2022) 131183.

[41] L. Xu, Y. Zhang, L. Feng, X. Li, Q. An, A facile preparation method for MoS2 nanosheets and their well-controllable interfacial assembly with PEDOT: PSS for effective electrochemical hydrogen evolution reactions, J. Mater. Sci. 56 (2021) 7008–7021.

[42] Y. Zhu, S. Ding, X. Wang, R. Zhang, X. Feng, X. Sun, G. Xiao, Y. Zhu, Interfacial electronic interaction in In2O3/Poly(3,4-ethylenedioxythiophene)-modified carbon heterostructures for enhanced electroreduction of CO2 to formate, ACS Appl. Mater. Interfaces 15 (28) (2023) 33633–33642.

[43] A.V. Volkov, K. Wijeratne, E. Mitraka, U. Ail, D. Zhao, K. Tybrandt, J.W. Andreasen, M. Berggren, X. Crispin, I.V. Zozoulenko, Understanding the capacitance of PEDOT: PSS, Adv. Funct. Mater. 27 (28) (2017) 1700329.

[44] Y. Jiang, X. Dong, L. Sun, T. Liu, F. Qin, C. Xie, P. Jiang, L. Hu, X. Lu, X. Zhou, W. Meng, N. Li, C.J. Brabec, Y. Zhou, An alcohol-dispersed conducting polymer complex for fully printable organic solar cells with improved stability, Nat. Energy 7 (2022) 352–359.

[45] J. Rivnay, S. Inal, B.A. Collins, M. Sessolo, E. Stavrinidou, X. Strakosas, C. Tassone, D.M. Delongchamp, G.G. Malliaras, Structural control of mixed ionic and electronic transport in conducting polymers, Nat. Commun. 7 (2016) 11287.

[46] B.D. Paulsen, K. Tybrandt, E. Stavrinidou, J. Rivnay, Organic mixed ionic-electronic conductors, Nat. Mater. 19 (2020) 13–26.

[47] R. del Olmo, T.C. Mendes, M. Forsyth, N. Casado, Mixed ionic and electronic conducting binders containing PEDOT:PSS and organic ionic plastic crystals toward carbon-free solid-state battery cathodes, J. Mater. Chem. A 10 (2022) 19777–19786.

[48] R. Wu, M. Matta, B.D. Paulsen, J. Rivnay, Operando characterization of organic mixed ionic/electronic conducting materials, Chem. Rev. 122 (2022) 4493–4551.

[49] W. Shi, T. Zhao, J. Xi, D. Wang, Z. Shuai, Unravelling doping effects on PEDOT at the molecular level: from geometry to thermoelectric transport properties, J. Am. Chem. Soc. 137 (40) (2015) 12929–12938.

[50] W. Michaels, Y. Zhao, J. Qin, Atomistic modeling of PEDOT:PSS complexes I: DFT benchmarking, Macromolecules 54 (2021) 3634–3646.

[51] R. Balu, N.R. Choudhury, J.P. Mata, L. de Campo, C. Rehm, A.J. Hill, N.K. Dutta, Evolution of the interfacial structure of a catalyst ink with the quality of the dispersing solvent: a contrast variation small-angle and ultrasmall-angle neutron scattering investigation, ACS Appl. Mater. Interfaces 11 (10) (2019) 9934–9946.

[52] T.T. Ngo, T.L. Yu, H.L. Lin, Influence of the composition of isopropyl alcohol/water mixture solvents in catalyst ink solutions on proton exchange membrane fuel cell performance, J. Power Sources 225 (2013) 293–303.

[53] H. Yuk, B. Lu, S. Lin, K. Qu, J. Xu, J. Luo, X. Zhao, 3D printing of conducting polymers, Nat. Commun. 11 (2020) 1604.

[54] T. Mochizuki, K. Kakinuma, M. Uchida, S. Deki, M. Watanabe, K. Miyatake, Temperature- and humidity-controlled SAXS analysis of proton-conductive ionomer membranes for fuel cells, ChemSusChem 7 (3) (2014) 729–733.

[55] T. Lazaridis, B.M. Stühmeier, H.A. Gasteiger, H.A. El-Sayed, Capabilities and limitations of rotating disk electrodes versus membrane electrode assemblies in the investigation of electrocatalysts, Nat. Catal. 5 (2022) 363–373.

[56] M.B. Stevens, L.J. Enman, A.S. Batchellor, M.R. Cosby, A.E. Vise, C.D.M. Trang, S.W. Boettcher, Measurement techniques for the study of thin film heterogeneous water oxidation electrocatalysts, Chem. Mater. 29 (1) (2016) 120–140.

[57] A. Karmakar, S. Kundu, A concise perspective on the effect of interpreting the double layer capacitance data over the intrinsic evaluation parameters in oxygen evolution reaction, Mater. Today Energy 33 (2023) 101259.

[58] A. Halder, C. Liu, Z. Liu, J.D. Emery, M.J. Pellin, L.A. Curtiss, P. Zapol, S. Vajda, A.B.F. Martinson, Water oxidation catalysis via size-selected iridium clusters, J. Phys. Chem. C 122 (2018) 9965–9972.

[59] Y. Qin, T. Yu, S. Deng, X.Y. Zhou, D. Lin, Q. Zhang, Z. Jin, D. Zhang, Y.B. He, H.J. Qiu, L. He, F. Kang, K. Li, T.Y. Zhang, RuO2 electronic structure and lattice strain dual engineering for enhanced acidic oxygen evolution reaction performance, Nat. Commun. 13 (2022) 3784.

[60] C. Rong, K. Dastafkan, Y. Wang, C. Zhao, Breaking the activity and stability bottlenecks of electrocatalysts for oxygen evolution reactions in acids, Adv. Mater. 35 (49) (2023) 2211884.

[61] S. Ott, A. Orfanidi, H. Schmies, B. Anke, H.N. Nong, J. Hübner, U. Gernert, M. Gliech, M. Lerch, P. Strasser, Ionomer distribution control in porous carbon-supported catalyst layers for high-power and low Pt-loaded proton exchange membrane fuel cells, Nat. Mater. 19 (2019) 77–85.

[62] T. Asano, S. Yubuchi, A. Sakuda, A. Hayashi, M. Tatsumisago, Electronic and ionic conductivities of $LiNi_{1/3}Mn_{1/3}Co_{1/3}O_2$-$Li_3PS_4$ positive composite electrodes for all-solid-state lithium batteries, J. Electrochem. Soc. 164 (2017) A3960–A3963.

[63] J. Li, H. Tang, R. Chen, D. Liu, Z. Xie, M. Pan, S.P. Jiang, Highly ordered 3D macroporous scaffold supported Pt/C oxygen electrodes with superior gas-proton transportation properties and activities for fuel cells, J. Mater. Chem. A 3 (2015) 15001–15007.

[64] S. Zhao, Y. Liao, R. Wang, G. Liu, H. Zhang, H. Tang, Polyphenol synergistic cerium oxide surface engineering constructed core-shell nanostructures as antioxidants for durable and high-performance proton exchange membrane fuel cells, Chem. Eng. J. 472 (2023) 144804.

[65] H. Ren, Y. Teng, X. Meng, D. Fang, H. Huang, J. Geng, Z. Shao, Ionomer network of catalyst layers for proton exchange membrane fuel cell, J. Power Sources 506 (2021) 230186.

Neng Li, Fellow of Royal Society of Chemistry (FRSC), is a full professor in the State Key Laboratory of Silicate Materials for Architectures, Wuhan University of Technology. He received Ph.D. degree in 2011 from the Huazhong University of Science and Technology. He worked at University of Cambridge as a Research Fellow in 2016–2017. His current research interests focus on amorphous materials, and energy conversion and storage materials. He has published >300 peer-reviewed papers, with H-index of 68. He serves on the editorial boards/young advisory board of Materials Horizons, Advanced Powder Materials, Journal of Inorganic Materials, Acta Physico-Chimica Sinica, etc.

Haolin Tang is a full professor in the State Key Laboratory of Advanced Technology for Materials Synthesis and Processing, Wuhan University of Technology. He obtained his BSc degree in Chemistry (2001) and his PhD in Material (2007) at WUT. Then he worked as a Research Fellow at NTU, Singapore (2008). In 2011 he was appointed as a full professor of material science at WUT. He has published >290 peer-reviewed papers, with H-index of 54. He is an Editorial Board Member of several international Journals such as Advanced Composites and Hybrid Materials, Energies and Polymers. His research interests include fuel cells, solid electrolytes, electrochemistry of nanomaterials, and self-assembly of nanocomposites.

Liyan Zhu obtained her bachelor's degree at Henan Polytechnic University in 2021. She is currently pursuing her master's degree at Wuhan University of Technology, under the supervision of Prof. Haolin Tang. Her current research interests focus on proton exchange membrane water electrolysis.